PAPER • OPEN ACCESS

Broadband subwavelength tunable valley edge states induced by fluid filling acoustic metastructure

To cite this article: Tao Yang *et al* 2022 *J. Phys. Commun.* **6** 065003

View the article online for updates and enhancements.

Journal of Physics Communications

PAPER

Broadband subwavelength tunable valley edge states induced by fluid filling acoustic metastructure

Tao Yang[1,2], Meng Chen[1,2,*] ⓘ, Yu Liu[1,2], Boya Xiao[1,2], Xilin Wang[3], Dongliang Pei[1,2], Heng Jiang[1,2,*] ⓘ and Yuren Wang[1,2]

1   Key Laboratory of Microgravity, Institute of Mechanics, Chinese Academy of Sciences, Beijing 100190, People's Republic of China
2   University of Chinese Academy of Sciences, Beijing, 100049, People's Republic of China
3   Beijing Information Science and Technology University, 100192, People's Republic of China
*   Authors to whom any correspondence should be addressed.

E-mail: chenmeng@imech.ac.cn and hengjiang@imech.ac.cn

Abstract

Topological acoustic insulators demonstrate unusual characteristics in manipulating sound wave, which attract much attention from researchers. However, most of the recent researches are based on passive system, hampering their dispersion tunability. In this paper, a broadband subwavelength tunable fluid filling acoustic topological metastructure is studied. It is composed of perforated cells with tunable water height in the hole, which enables the dispersion of the edge state to be tuned. The inversion symmetry is broken by expanding and shrinking the adjacent holes in the unit cell. Thus, the valley Hall states with opposite Chern number form at the K point in the Brillouin zone. The edge states emerge at the boundary of the different valley Hall phases. The robustness of the edge states is verified by the straight and Z-shaped waveguide. Furthermore, the dispersion of the edge state can be altered continuously by raising and reducing the water height, giving rise to broadband variable topological states, which greatly expands the bandwidth from 40 Hz to 1033 Hz. This work offers a new method to control the topological states and shows great potential for practical application.

1. Introduction

Topological insulators [1, 2] originated from the condensed matter physics have aroused great interests in acoustical field. It enables acoustic wave to propagate unidirectionally along the edge of the surface being immune to the defects such as cavity, dislocation and sharp corners, which outlines a promising prospect in sound communication and noise control. Due to the macroscopic controllability, it is convenient and direct to observe the topological state in the acoustic system. The topological states form along the interfaces by emulating the quantum Hall effect (QHE) [3, 4], quantum spin Hall effect (QSHE) [5, 6] and quantum Valley Hall effect (QVHE) [7, 8]. Generally, the key to realizing acoustic analogue QHE is to break time-reversal symmetry with the introduced external field. Researchers [9–12] apply the circulating fluid into acoustic ring resonators to achieve non-reciprocity, giving rise to time-reversal symmetry broken. As for acoustic analogue QSHE, it is the crux of the matter to increase the degree of freedom of the system and build up pseudospin states. Studies [13–15] show that the QSHE can be realized by changing the filling ratio within the honeycomb unit cell thanks to the inversion of acoustic energy band at a double Dirac cone. With regard to the acoustic analogue QVHE, only the inversion-symmetry broken is required. Schemes [16–20] are applied to break the inversion symmetry by rotating the scatters or changing the eigenfrequency of adjacent metamolecules to achieve valley states or multiple classes of topological modes within a single platform. Although many of these works have achieved significant milestones, their invariant dispersion of topological states which exist in the topological band gap limits them greatly since the geometric parameters of the unit cell cannot be altered once fabricated. Therefore, it is desirable to make it possible to tune the dispersion of topological states for these systems.

It is noted that there are many effective strategies to realize dispersion tunability in acoustic metamaterials (AMs). Vast majority of AMs fall into two classes [21–23]: passive AMs and active AMs. The former is usually accessible to specific frequencies once the unit cell is fabricated, resulting in fixed dispersion. The latter offers the opportunity of adjustable dispersion at wide frequency range by introducing an additional degree of freedom, such as piezoelectric control [24, 25], mechanical control [26–30], electronic control [31, 32], magnetic control [33, 34] and temperature control [35]. In essence, realizing dispersion tunable topological systems is similar to the tunable metamaterials. However, a few of these strategies are applied to the topological acoustic systems [36–39]. One way is to generate the deformation to affect the band gap width based on a strain-driven mechanism [36]. Another way is to configurate the structure by employing shunted piezoelectric (PZT) disks in which the systems' mechanical impedance can be altered [37]. Above all, these methods do realize the dispersion tunability of topological states, but it is still difficult for them to vary the dispersion of the edge state continuously over the broad frequency range. In a word, the reason for this is that these topological systems are based on passive system and their unit cell size and configuration remain unchanged during the modulation. In light of that, the active continuous tunability of topological state dispersion over broadband is highly demanded. It is noteworthy that some strategies have been applied to achieve continuous tunability. Tian *et al* [17] paved a way to tune the dispersion of edge states continuously by enlarging or shrinking the air channel height. Mazzotti *et al* [21] applied compression or tension to the unit cell to lead to continuous shift in the bandgap. Miniaci *et al* [40] realized the continuously tunable dispersion by employing an external prestress.

In order to solve above challenges, we focus not only on active continuous tunability, but also on broadband. Considering the lattice size remains the same during the modulation, the passive system is not applicable and the active system which is not limited by the lattice size is needed. In acoustic metamaterials the dispersions generated by local resonance are not associated with the lattice size, which provides a feasible strategy to construct the continuously tunable system. To simplify the system, the single-phase materials based on resonator outweigh the multiphase materials. Therefore, we construct the configuration by modeling a honeycomb lattice made of the perforated unit cells. The eigenfrequency of the unit cell is influenced by the air column height within the hole. Given this, the continuous tunability over broadband can be realized only through varying the air column height gradually. Due to the impedance mismatch between air and water, water filling system would be suitable to tune the air column height. Therefore, the variable air column height can be achieved by varying the water height in the water tank. Moreover, the inversion-symmetry broken occurs by changing the geometry of the adjacent holes, which gives rise to the topological phase transition characterized by valley Chern numbers. The topological states form along the interfaces with different valley Hall phases and its dispersion can be continuously tuned by increasing or reducing the volume of water. Finally, we have verified the robust edge state along the interfaces with tunable frequency through simulations and experiments. Contrast to the previous scheme, this kind of design can tune the dispersion continuously over broadband, which greatly expands the bandwidth from 40 Hz to 1033 Hz. It is conducive to extend the topological insulator to the practical application.

2. Models and methods

Figure 1 shows the fabricated topological acoustic system which is composed of an acrylic ceiling and a perforated rigid material made of nylon in which holes are distributed in a honeycomb lattice. In this way, acoustic waves are confined in a 2D space between the ceiling and the rigid material. The perforation depth and the radius of the holes are h = 6 cm, R = 1 cm, respectively. The height between the ceiling and the rigid material is H = 5 cm. There are two holes distributed in the unit cell with the lattice constant $a = 3\sqrt{3}$ cm. The center-to-center distance between the two adjacent holes is $L = \frac{\sqrt{3}}{3}a$. The honeycomb lattice with same radius hole is to be considered as C_{3v} symmetry, while the lattice with different radius hole is to be considered as C_3 symmetry, which breaks the inversion symmetry and is marked by the red dashed line in figure 1. The air column height in holes is h_a, which can be controlled by the volume of the water. The standard material parameters of the perforated nylon material are as below: the longitudinal velocity $v_1 = 2591$ m s^{-1} and the mass density $\rho_1 = 1070$ kg m^{-3}. The sound velocity and mass density of air is $c_0 = 343$ m s^{-1} and $\rho_0 = 1.29$ kg m^{-3}, for water are $c_2 = 1500$ m s^{-1} and $\rho_2 = 1000$ kg m^{-3}.

Simulations are modeled with the air domain of the unit cell utilizing the finite-element software COMSOL Multiphysics. When the radius of the adjacent holes is the same (R = 10 mm) and $h_a = h$, the dispersion of the whole system is shown in figure 2 (a) marked by black solid line. Because of the protection of the inversion symmetry (C_{3V}) the subwavelength Dirac cone is formed at the K, K' point of the Brillouin zone at 1273 Hz, with its normalized frequency $f_n = 0.193$ ($f_n = f \cdot a/c_0$). Note that the Dirac cone formed below the sound line (marked by yellow dashed line), indicating that the propagation of spoof SAWs confined in the holes [41]. Later, the degeneracy at K, K' point of the Brillouin zone is lifted to generate a bandgap by breaking the inversion
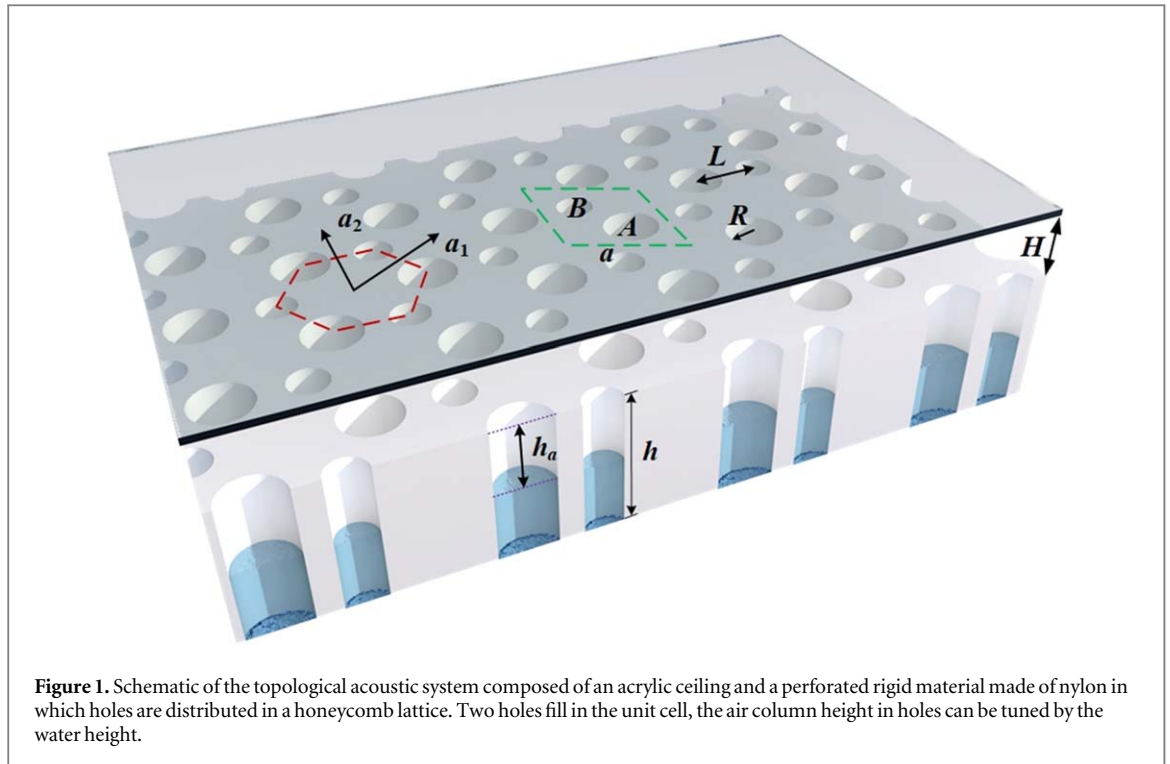
Figure 1. Schematic of the topological acoustic system composed of an acrylic ceiling and a perforated rigid material made of nylon in which holes are distributed in a honeycomb lattice. Two holes fill in the unit cell, the air column height in holes can be tuned by the water height.
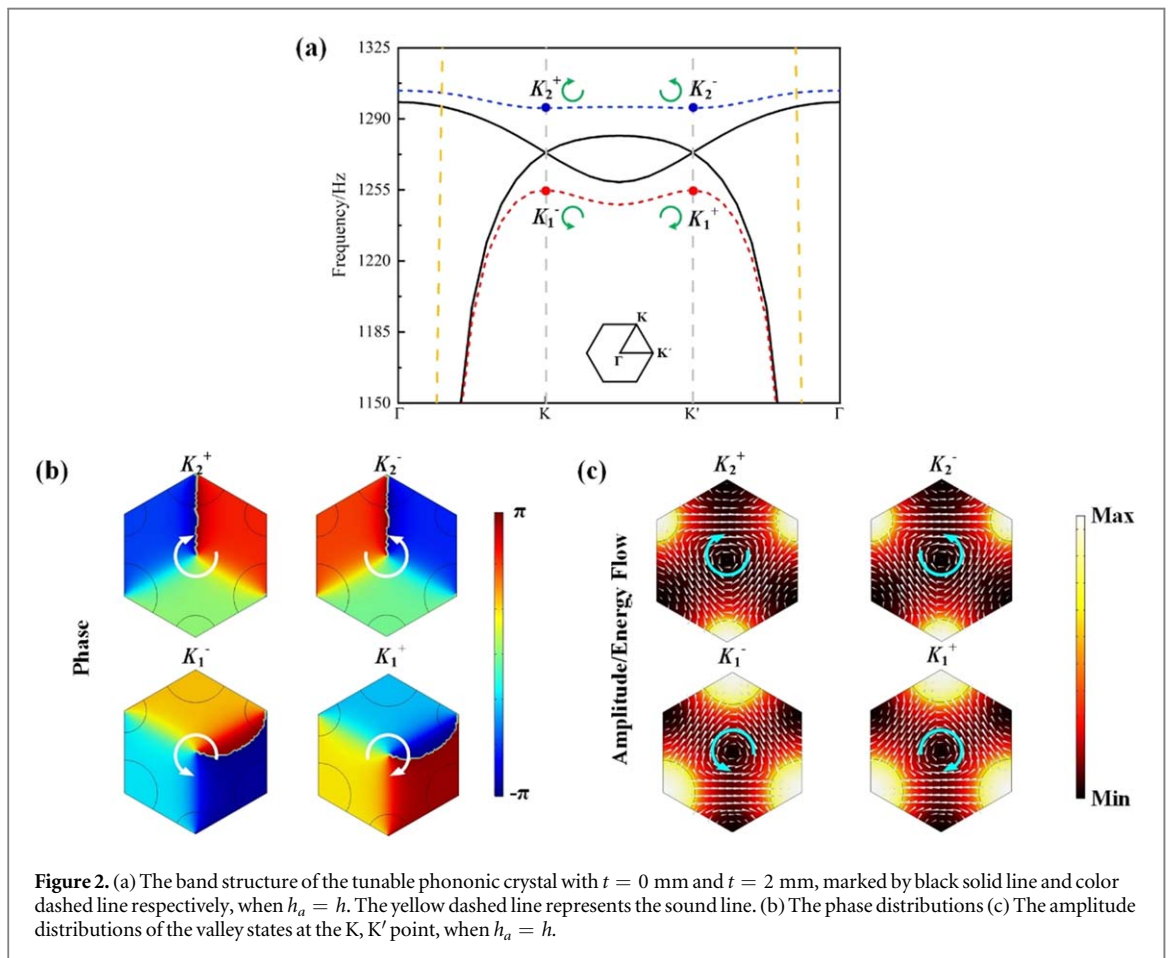
Figure 2. (a) The band structure of the tunable phononic crystal with $t = 0$ mm and $t = 2$ mm, marked by black solid line and color dashed line respectively, when $h_a = h$. The yellow dashed line represents the sound line. (b) The phase distributions (c) The amplitude distributions of the valley states at the K, K′ point, when $h_a = h$.

symmetry (C_3). Here we expand and shrink the radius of the adjacent holes in unit cell by the same size ($t = 2$ mm). Thus, the radius of hole A is expanded to 12 mm ($R + t$) and the radius of hole B is shrunk to 8 mm ($R - t$). The dispersion of the system with inversion symmetry broken is shown in figure 2(a) marked by color

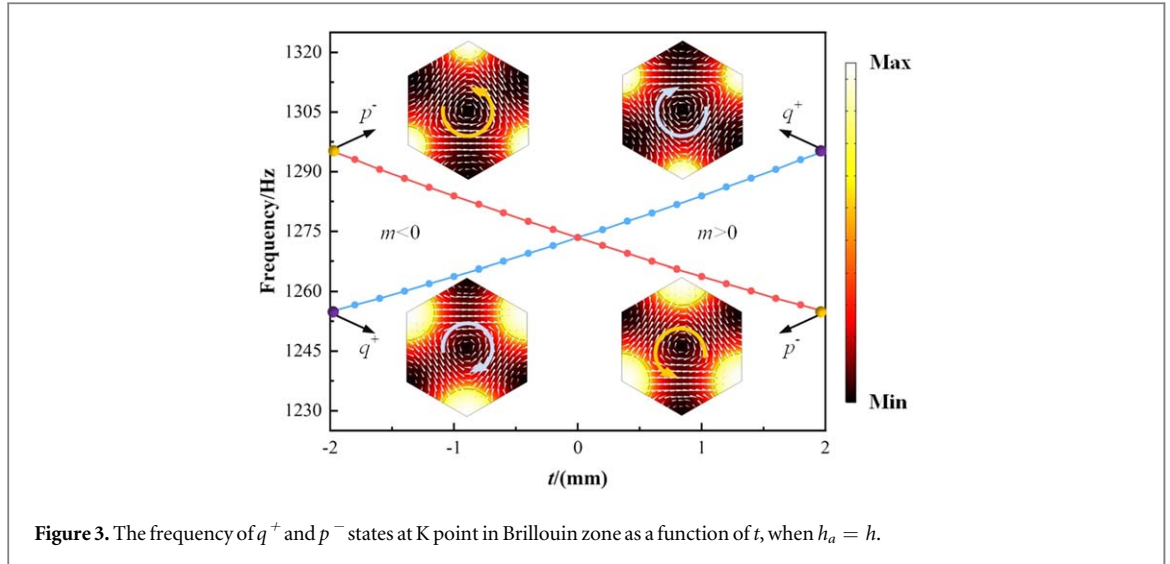**Figure 3.** The frequency of q^+ and p^- states at K point in Brillouin zone as a function of t, when $h_a = h$.

dashed line. There are two pairs of valley states with energy extrema located at the upper and lower boundary of the bandgap at point K, K′ in momentum space, which are denoted by K_1^-, K_1^+, K_2^- and K_2^+. The bandgap spans from 1255 Hz to 1295 Hz with 40 Hz bandwidth. To better understand the physical picture of the valley states, the phase and amplitude distributions of the valley state are demonstrated in figures 2(b) and (c), respectively. As for point K, the K_2^+ and K_1^- valley states own clockwise and anticlockwise vortex directions respectively, which is embodied in the superscript symbol '+' and '−'. These two acoustic valley states share opposite chirality similar to electron spin states. As for point K′, the time-reversal of point K, it is the same for valley states K_2^- and K_1^+. Due to the time reversal symmetry, the vortex direction of the valley state at K, K′ point also shares opposite chirality.

3. Results and discussion

3.1. Topological phase transition

To display the acoustic valley Hall transition, the continuous evolution of the band-edge frequencies mode q^+ and p^- versus the radius variation t is plotted in figure 3. Mode q^+ and p^- indicate clockwise and anticlockwise energy flow separately. With the increase of the absolute value of t, the radius difference between adjacent holes gradually becomes larger, resulting in the enlargement of band gap by degrees. When $t = 0$, the radius of adjacent holes are exactly the same and two different pseudospin valley states intersect, which leads to the degeneracy of point K in momentum space. As the radius variation t changing from −2 mm to 2 mm, the subwavelength band gap experienced closure and reopening. The pressure field distributions and energy flows of q^+, p^- states at $t = -2$ mm and $t = 2$ mm are shown in figure 3. It is obvious to find that the vortex chirality of valley state is inverted from $t < 0$ to $t > 0$. Furthermore, the position of q^+, p^- at the K point in band structure is also exchanged during this process, which presents the process of band inversion.

In order to display the topology characteristics of the band, the non-zero Valley Chern number and the k-p perturbation method are introduced. The topological phase transition can be captured by a t-dependent continuum Hamiltonian [16]:

$$\delta H = v_D \delta k_x \sigma_x + v_D \delta k_y \sigma_y + m v_D^2 \sigma_z \tag{1}$$

Where v_D is the Dirac velocity of the conic dispersion at $t = 0$ mm, $\delta k = (\delta k_x, \delta k_y)$ is the momentum deviation from the K point, and σ_i are the Pauli matrices of the vortex pseudospins. The effective mass characterizes two different valley states with opposite vortices:

$$m = \Delta\omega / 2v_D^2 \tag{2}$$

where the bandwidth $\Delta\omega = \omega_{q^+} - \omega_{p^-}$, so the effective Hamiltonian depends strongly on t. The local Berry curvature $\Omega(\delta k)$ centered at the K valley can be calculated by using the eigenvector, and topological charges can be calculated by integrating the local Berry curvature:

$$C_K = \frac{1}{2\pi} \int \Omega(\delta k) dS = \frac{1}{2} \operatorname{sgn}(m) \tag{3}$$

The Chern number of the upper band are $-\frac{1}{2}\left(\frac{1}{2}\right)$ at valley K(K′) for a domain with $t < 0$ ($m < 0$) and $\frac{1}{2}\left(-\frac{1}{2}\right)$ at valley K(K′) for a domain with $t > 0$ ($m > 0$).

Thus, the topological phase transition occurs in conjunction with a change of the valley Chern number at $t = 0$ mm, which predicts that the edge states propagate along the interface between the two honeycomb lattices with opposite t.
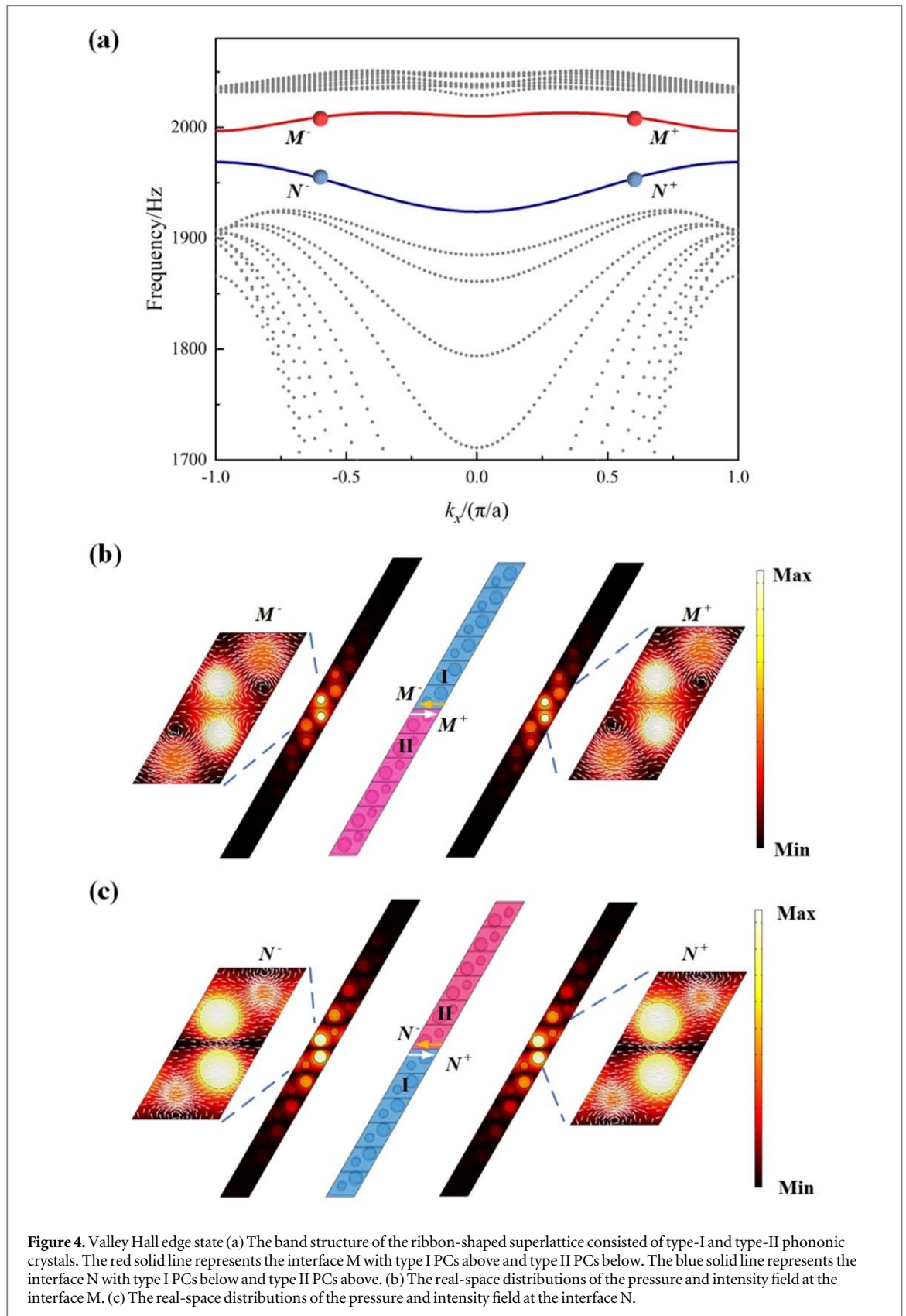
3.2. Edge states

Based on above analysis, there are two different valley Hall phases which are consisted of unit cells with different *t*. These two types of structure are denoted by I, II respectively. Applying them, a ribbon-shaped supercell is constructed, as shown in figure 4. Two different types of interfaces can be formed through exchanging the upper and lower position of these two types of PCs. The interface M is obtained with type II above and type I below and interface N is in reverse order. In order to obtain the band structure of the supercell, the periodic boundary condition is imposed along the left and right boundary and the perfectly matched layer is applied along the upper and lower boundary of the supercell.

From the derived dispersion relations (figure 4(a)) for $h_a = 0.6$ h, the edge modes at interface M and N are formed amongst the bandgap, which are denoted by red and blue solid lines respectively. Points M^-, M^+, N^-, N^+ represent the edge states propagating along the interface of M and N. Point M^- and N^- are located at the band gap with the value of momentum $k_x = \frac{3\pi}{5a}$, point M^+ and N^+ are located at the band gap with the value of momentum $k_x = -\frac{3\pi}{5a}$. The real-space distributions of the pressure and intensity field at points M^-, M^+, N^-, N^+ are shown in figures 4(a), (b). We can find that the pressure field is confined at the interface and decays exponentially into bulk crystals. Also, the Poynting vectors indicate that the edge states are unidirectional at the interface between different topological regions. There are two edge modes with opposite propagation direction at interface M and N. It can be derived that the boundary state is a spiral boundary mode similar to the valley pseudospin of the electronic system.

Later, add or reduce the volume of water to change the air column height h_a in holes, the edge state dispersion can be tuned. It is demonstrated in figure 5(a), the frequency of the edge mode increases with the decrease of h_a, that is, the air column height becomes shorter. Since the topological acoustic system is based on the local resonant mechanism, the air column height affects the resonant frequency of the system. Given this, the topological bandgap can be tuned to different frequency range so that the edge state occurs at different frequency range by changing the volume of water. Furthermore, the dispersion of edge states can also be tuned by changing the height between the ceiling and the rigid materials H. It is demonstrated in figure 5(b). The frequency of the edge states is greatly affected by the H when it comes to lower channel height H. When H gradually increases, the frequency of the edge states varies slightly.

In order to show the transportation of the edge state, we design a straight waveguide in a $16a \times 20a$ lattice and a Z-shaped waveguide in a $16a \times 20a$ lattice composed of type-I and type-II phononic crystals, as shown in figures 6(a) and (b), respectively. The acoustic wave emitted by a point source illuminates the waveguides from the left side. The air column height in these two waveguides is set to be 0.6 h. It can be seen from figure 6(a) that the sound wave only propagates along the interface between these two types of phononic crystals at 1956Hz and decays exponentially into the bulk, which confirms the existence of the edge state at the topological interface. To further test the robustness of the edge state, the sharp corners are introduced into the waveguide. In figure 6(b), the sound wave propagates smoothly in the Z-shaped channel, even at the two sharp corners. To demonstrate the immunity to backscattering around the sharp corner, there are different methods [16, 37, 42] to prove it. Here, we have derived the power transmission and reflection spectra from the sharp corners through a one-dimensional scattering matrix method [16]. It shows in figure 6(c), during the frequency range of edge state there is weak backscattering, which indicates the backscattering-free of the edge state along the topological boundary. Also, the edge state along the topological interface can be tuned continuously through changing the volume of water in the holes. Figure 6(d) shows the edge state frequency of the straight waveguide system varies with air column height h_a continuously. As h_a changes from h to 0.5 h the frequency of the edge state ranges from 1257 Hz to 2290 Hz, with 1033 Hz bandwidth. Consequently, the sound wave can propagate along any path at the topological boundary with backscattering-free and robust propagation, at the same time the edge state can be tuned continuously over broadband.

To verify the backscattering-free transmission of topological edge state and continuous tunability, the straight waveguide is fabricated. It is in a finite $16a \times 20a$ lattice, which is made of nylon, as shown in figure 7(a). The topological interface in straight waveguide is denoted by the blue dashed line. During the experiment, the whole structure is placed in a water tank with the same shape, in order to reduce the impact of noise, an acrylic glass is placed upon the structure. The speaker (Brüel & Kjær-4295) driven by a power amplifier is placed at the right end as a point sound source. A 1/4-inch microphone (Brüel & Kjær-4966) is set to the port A, B to collect the edge state and bulk state sound pressure signal respectively and acoustic intensity at each position can be retrieved by using the PULSE

Figure 4. Valley Hall edge state (a) The band structure of the ribbon-shaped superlattice consisted of type-I and type-II phononic crystals. The red solid line represents the interface M with type I PCs above and type II PCs below. The blue solid line represents the interface N with type I PCs below and type II PCs above. (b) The real-space distributions of the pressure and intensity field at the interface M. (c) The real-space distributions of the pressure and intensity field at the interface N.

Reflex software. Figures 7(b) and (c) illustrate the simulated and experimentally measured transmission spectra of acoustic waves through the straight waveguides with $h_a = 0.6$ h. The red solid line stands for the edge state, and the blue solid line stands for the bulk state. Figure 7(c) shows the measured ~10 dB transmission enhancement of edge state as compared to the bulk state both in the straight waveguide. Compared with the simulation results, the redshift in the experimentally measured transmission spectra comes from the following factors: 1. the capillary effect of the water tank, 2. inaccurate water height control, and 3. imperfectly flat bottom surface. Changing the water height in the
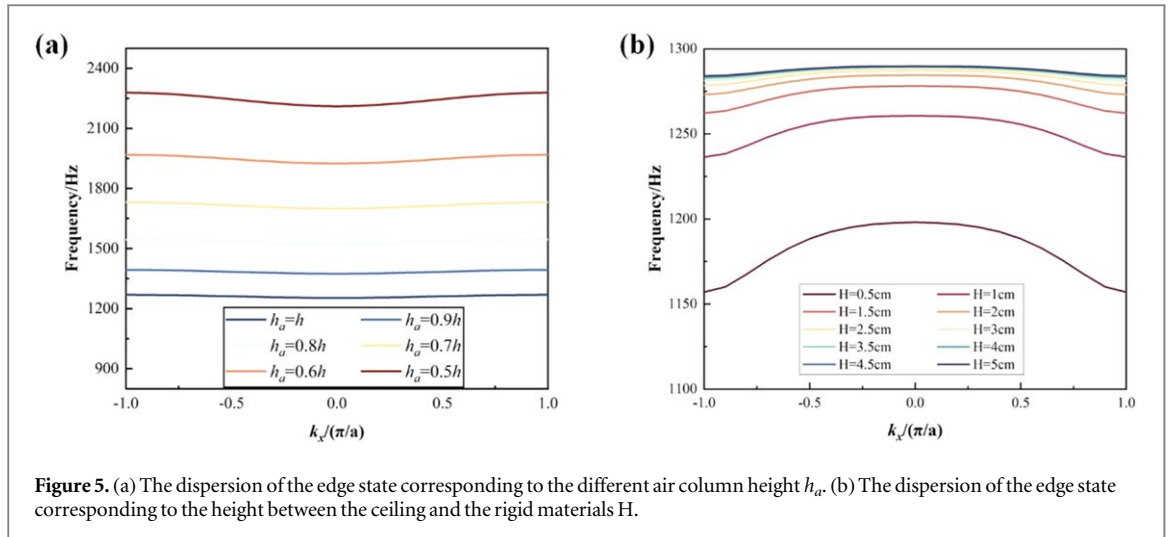
Figure 5. (a) The dispersion of the edge state corresponding to the different air column height h_a. (b) The dispersion of the edge state corresponding to the height between the ceiling and the rigid materials H.
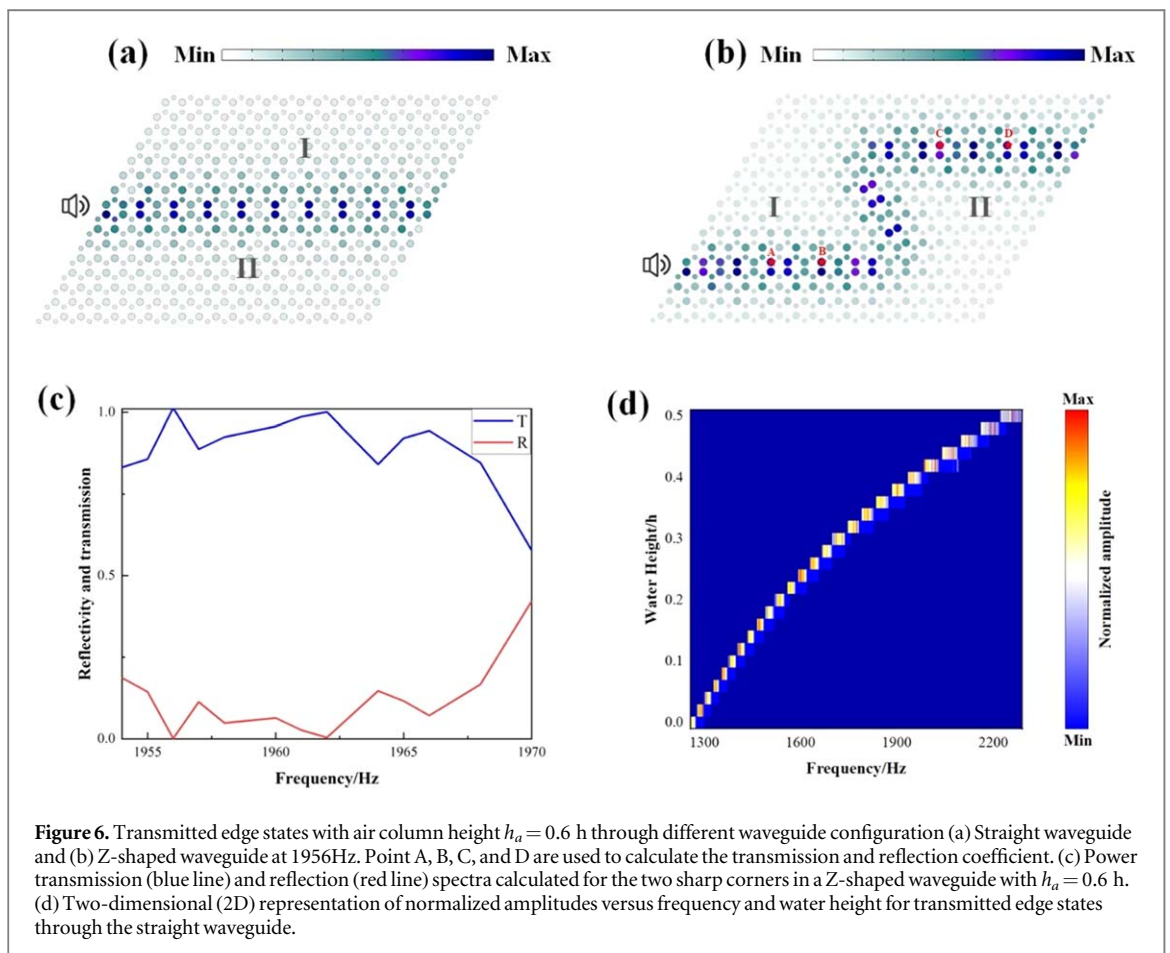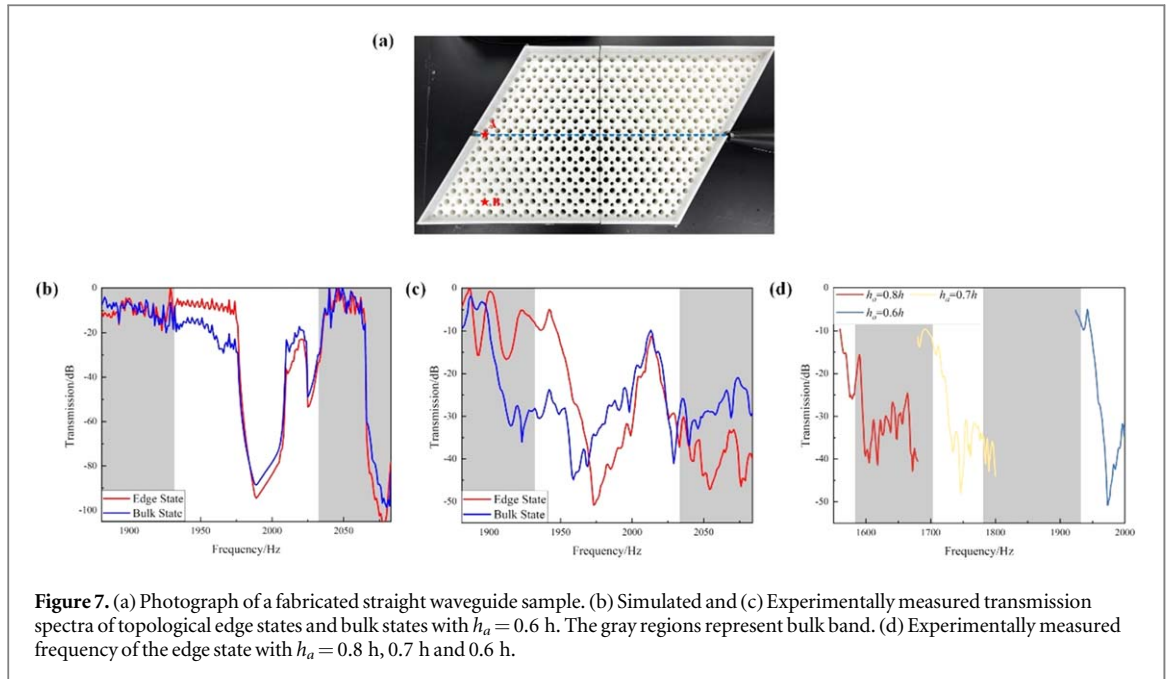

Figure 6. Transmitted edge states with air column height $h_a = 0.6$ h through different waveguide configuration (a) Straight waveguide and (b) Z-shaped waveguide at 1956Hz. Point A, B, C, and D are used to calculate the transmission and reflection coefficient. (c) Power transmission (blue line) and reflection (red line) spectra calculated for the two sharp corners in a Z-shaped waveguide with $h_a = 0.6$ h. (d) Two-dimensional (2D) representation of normalized amplitudes versus frequency and water height for transmitted edge states through the straight waveguide.

water tank so that the edge states can be tuned. Figure 7(d) shows the transmission curves of edge states with h_a = 0.8 h, 0.7 h and 0.6 h. The frequency of the edge state increases gradually with the rise of the water height. It verifies the edge states can be tuned continuously by changing water height. Thus, this straight channel holds topological edge state and the dispersion of the edge state can be tuned continuously by changing the water height, which is in good agreement with the simulation.

4. Conclusion

In this paper, we construct a broadband continuously tunable topological acoustic system made of perforated unit cells. Due to the introduced local resonance, the eigenfrequency of the unit cell is affected by the air column

Figure 7. (a) Photograph of a fabricated straight waveguide sample. (b) Simulated and (c) Experimentally measured transmission spectra of topological edge states and bulk states with $h_a = 0.6$ h. The gray regions represent bulk band. (d) Experimentally measured frequency of the edge state with $h_a = 0.8$ h, 0.7 h and 0.6 h.

height in the holes. At the point K in the first Brillouin zone, a subwavelength Dirac cone forms attributed to the C_{3V} symmetry of the system. By changing the radius of the adjacent holes, the inversion symmetry is broken and the topological band gap forms. There are two pairs of valley states existing at the boundary of the band gap with opposite chirality. Furthermore, the topological phase transition is confirmed by calculating the band structure, energy flow and valley Chern numbers. In addition, the edge state one-way transmission at the interface between two types of structure with different valley Chern numbers is verified by simulations and experimental results, which shows the edge state stably propagates in the Z-shaped channel and is not affected by backscattering and defects. Through changing the volume of water in the holes the dispersion of the edge state can be tuned continuously. The air column height varies from h to 0.5 h, the frequency of the edge state ranges from 1257 Hz to 2290 Hz with bandwidth 1033 Hz. It greatly expands the frequency band of topological states from 40 Hz bandwidth to 1033 Hz bandwidth. This kind of topological acoustic system provides a new way to control the sound waves precisely.
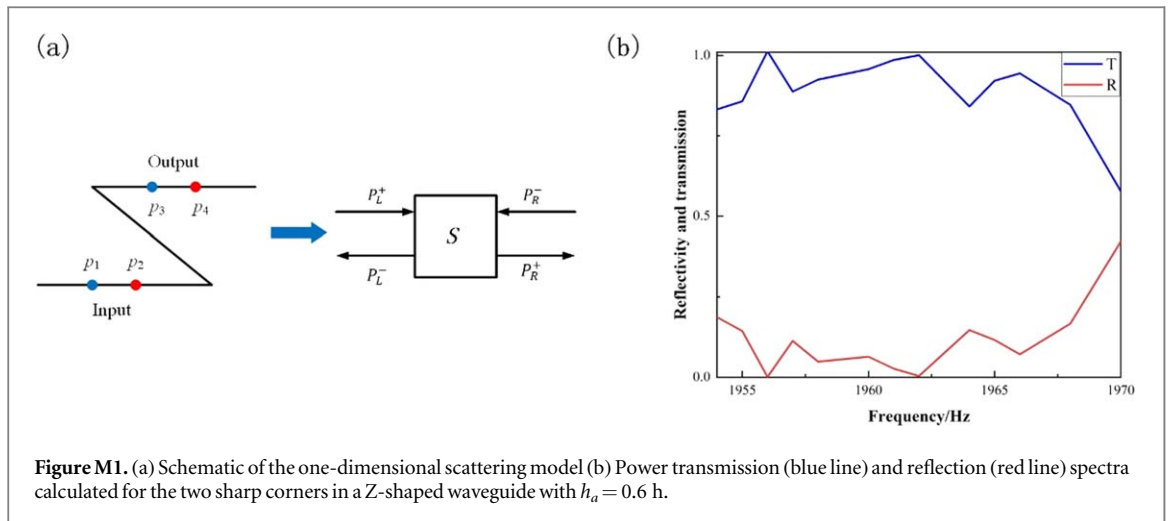
4.1. Method
4.1.1. Tuning the water height
The method we proposed to tune the water height is manual. There is a scale on the wall of the water tank, the water height can be varied continuously by adding or reducing the volume of water with a measuring cylinder. However, it is possible to make the whole system programmable by adding the microcontroller and laser rangefinder.

4.1.2. Power reflection and transmission spectra
To unequivocally prove the backscattering-free topological transmissibility around the two sharp corners, we have carefully calculated the power transmission and reflection spectra for the two sharp corners in Z-shaped waveguide with $h_a = 0.6$ h through a one-dimensional scattering matrix method [16]. Figure M1(a) shows the one-dimensional scattering model. The sharp corners together can be considered as a black box connecting the input and output channels. In this model, $p_1 = p_L^+ + p_L^-$ and $p_2 = p_L^+ e^{i\varphi} + p_L^- e^{-i\varphi}$, in which p_L^+ and p_L^- stand for the forward and backward acoustic waves, respectively. The phase term $\varphi = k_x l$, where l stands for the distance between the point p_1 and p_2 and k_x stands for the Bloch wavevector of the edge states. Given above relations, P_L^+ and P_L^- can be derived from p_1 and p_2. Similarly, P_R^+ and P_R^- can be derived from p_3 and p_4. Furthermore, the incident acoustic wave P_L^+ and P_R^- can be connected with the scattering wave P_L^- and P_R^+ through the scattering matrix.

$$\begin{pmatrix} P_L^- \\ P_R^+ \end{pmatrix} = S \begin{pmatrix} P_L^+ \\ P_R^- \end{pmatrix} \tag{S1}$$

Figure M1. (a) Schematic of the one-dimensional scattering model (b) Power transmission (blue line) and reflection (red line) spectra calculated for the two sharp corners in a Z-shaped waveguide with $h_a = 0.6$ h.

In a dissipationless system,

$$S = \begin{pmatrix} r & t \\ t & -r^*t/t^* \end{pmatrix}, \tag{S2}$$

where r and t represent the reflection and transmission coefficients, respectively. Combining equations (S1) and (S2), the power reflection and transmission can be derived.

Power reflection: $R = |r|^2$

Power transmission: $T = |t|^2$

Figure M1(b) shows the Power transmission (blue line) and reflection (red line) spectra for the two sharp corners in a Z-shaped waveguide with $h_a = 0.6$ h. It proves that the edge states' immunity to backscattering around the sharp corners during the frequency range of edge states.

Acknowledgments

Data availability statement

All data that support the findings of this study are included within the article (and any supplementary files).

ORCID iDs

Meng Chen ⓘ https://orcid.org/0000-0003-4141-7999
Heng Jiang ⓘ https://orcid.org/0000-0002-6552-2809

References

[1] Hasan M Z and Kane C L 2010 *Rev. Mod. Phys.* **82** 3045–67
[2] Qi X and Zhang S 2011 *Rev. Mod. Phys.* **83** 1057–110
[3] Klitzing K V, Dorda G and Pepper M 1980 *Phys. Rev. Lett.* **45** 494–7
[4] Laughlin R B 1983 *Phys. Rev. Lett.* **50** 1395–8
[5] Kane C L and Mele E J 2005 *Phys. Rev. Lett.* **95** 226801
[6] Andrei Bernevig B and Shou-Cheng Zhang T L H 2006 *Science* **314** 1757–61
[7] Yao W, Xiao D and Niu Q 2008 *Phys. Rev. B* **77** 235406
[8] Ju L *et al* 2015 *Nature* **520** 650–5
[9] Fleury R, Sounas D L, Sieck C F, Haberman M R and Alù A 2014 *Science* **343** 516–9
[10] Khanikaev A B, Fleury R, Mousavi S H and Alù A 2015 *Nat. Commun.* **6** 8260
[11] Souslov A, Van Zuiden B C, Bartolo D and Vitelli V 2017 *Nat. Phys.* **13** 1091–4
[12] Ding Y, Peng Y, Zhu Y, Fan X, Yang J, Liang B, Zhu X, Wan X and Cheng J 2019 *Phys. Rev. Lett.* **122** 014302
[13] He C, Ni X, Ge H, Sun X-C, Chen Y-B, Lu M-H, Liu X-P and Chen Y-F 2016 *Nat. Phys.* **12** 1124–9
[14] Zhang Z, Wei Q, Cheng Y, Zhang T, Wu D and Liu X 2017 *Phys. Rev. Lett.* **118** 084303

[15] Deng Y, Ge H, Tian Y, Lu M and Jing Y 2017 *Phys. Rev.* B **96** 184305

[16] Lu J, Qiu C, Ye L, Fan X, Ke M, Zhang F and Liu Z 2016 *Nat. Phys.* **13** 369–74

[17] Tian Z, Shen C, Li J, Reit E, Bachman H, Socolar J E S, Cummer S A and Jun Huang T 2020 *Nat. Commun.* **11** 762

[18] Yang Y, Yang Z and Zhang B 2018 *J. Appl. Phys.* **123** 091713

[19] Wang Z and Wei Q 2021 *J. Appl. Phys.* **129** 035102

[20] Miniaci M, Pal R K, Manna R and Ruzzene M 2019 *Phys. Rev.* B **100** 024304

[21] Mazzotti M, Bartoli I and Miniaci M 2019 *Front. Mater.* **6** 74

[22] Ji G and Huber J 2022 *Appl. Mater. Today.* **26** 101260

[23] Chen S, Fan Y, Fu Q, Wu H, Jin Y, Zheng J and Zhang F 2018 *Appl. Sci.* **8** 1480

[24] Casadei F, Delpero T, Bergamini A, Ermanni P and Ruzzene M 2012 *J. Appl. Phys.* **112** 064902

[25] Li Z *et al* 2017 *Sci Rep.* **7** 42863

[26] Lee K J B, Jung M K and Lee S H 2012 *Phys. Rev.* B **86** 184302

[27] Wang P, Casadei F, Shan S, Weaver J C and Bertoldi K 2014 *Phys. Rev. Lett.* **113** 014301

[28] Liu H, Wu J H and Ma F 2021 *J. Phys. D: Appl. Phys.* **54** 365105

[29] Chen Z, Shao S, Negahban M and Li Z 2019 *J. Phys. D: Appl. Phys.* **52** 395503

[30] Langfeldt F, Riecken J, Gleine W and von Estorff O 2016 *J. Sound Vib.* **373** 1–18

[31] Xiao S, Ma G, Li Y, Yang Z and Sheng P 2015 *Appl. Phys. Lett.* **106** 091904

[32] Ma G, Fan X, Sheng P and Fink M 2018 *Proc. Natl Acad. Sci. USA* **115** 6638–43

[33] Chen X, Xu X, Ai S, Chen H, Pei Y and Zhou X 2014 *Appl. Phys. Lett.* **105** 071913

[34] Borcea L and Bruno O 2001 *J. Mech. Phys. Solids* **49** 2877–919

[35] Xia B, Chen N, Xie L, Qin Y and Yu D 2016 *Appl. Acoust.* **112** 1–9

[36] Nguyen B H, Zhuang X, Park H S and Rabczuk T 2019 *J. Appl. Phys.* **125** 095106

[37] Darabi A, Collet M and Leamy M J 2020 *Proc. Natl Acad. Sci. USA* **117** 16138–42

[38] Dai H, Xia B and Yu D 2019 *J. Appl. Phys.* **125** 235105

[39] Liu X, Guo Q and Yang J 2019 *Appl. Phys. Lett.* **115** 074102

[40] Miniaci M, Mazzotti M, Amendola A and Fraternali F 2021 *Int. J. Solids Struct.* **216** 156–66

[41] Zhang Z, Gu Y, Long H, Cheng Y, Liu X and Christensen J 2019 *Research.* **2019** 1–8

[42] Miniaci M, Pal R K, Morvan B and Ruzzene M 2018 *Phys. Rev.* X **8** 031074